Title

Electrical signals in the ER are cell type and stimulus specific with extreme spatial compartmentalization in neurons

Journal
Cell Reports, 42(1)

ISSN
2639-1856

Authors
Campbell, Evan P
Abushawish, Ahmed A
Valdez, Lauren A
et al.

Publication Date
2023

DOI
10.1016/j.celrep.2022.111943

Published in final edited form as:
Cell Rep. 2023 January 31; 42(1): 111943. doi:10.1016/j.celrep.2022.111943.

Electrical signals in the ER are cell type and stimulus specific with extreme spatial compartmentalization in neurons

Evan P. Campbell[1], **Ahmed A. Abushawish**[1], **Lauren A. Valdez**[1], **Miriam K. Bell**[2], **Melita Haryono**[1], **Padmini Rangamani**[2], **Brenda L. Bloodgood**[1,3,*]

[1]Neurobiology Department, School of Biological Sciences, University of California San Diego, 9500 Gilman Drive, La Jolla, CA 92093, USA

[2]Department of Mechanical and Aerospace Engineering, University of California San Diego, 9500 Gilman Drive, La Jolla, CA 92093, USA

[3]Lead contact

SUMMARY

The endoplasmic reticulum (ER) is a tortuous organelle that spans throughout a cell with a continuous membrane containing ion channels, pumps, and transporters. It is unclear if stimuli that gate ER ion channels trigger substantial membrane potential fluctuations and if those fluctuations spread beyond their site of origin. Here, we visualize ER membrane potential dynamics in HEK cells and cultured rat hippocampal neurons by targeting a genetically encoded voltage indicator specifically to the ER membrane. We report the existence of clear cell-type- and stimulus-specific ER membrane potential fluctuations. In neurons, direct stimulation of ER ryanodine receptors generates depolarizations that scale linearly with stimulus strength and reach tens of millivolts. However, ER potentials do not spread beyond the site of receptor activation, exhibiting steep attenuation that is exacerbated by intracellular large conductance K^+ channels. Thus, segments of ER can generate large depolarizations that are actively restricted from impacting nearby, contiguous membrane.

Graphical abstract

---

[*]Correspondence: blbloodgood@ucsd.edu.

AUTHOR CONTRIBUTIONS
Conceptualization: E.P.C. and B.L.B. Methodology: E.P.C., M.K.B., P.R., and B.L.B. Formal analysis: E.P.C. and A.A.A. Investigation: E.P.C., A.A.A., L.A.V., and M.H. Resources: P.R. and B.L.B. Writing original draft: E.P.C., M.K.B., P.R., and B.L.B. Visualization: E.P.C., M.K.B., P.R., and B.L.B. Supervision: E.P.C., P.R., and B.L.B. Funding acquisition: P.R. and B.L.B.

SUPPLEMENTAL INFORMATION
Supplemental information can be found online at https://doi.org/10.1016/j.celrep.2022.111943.

INCLUSION AND DIVERSITY
One or more of the authors of this paper self-identifies as an underrepresented ethnic minority in their field of research or within their geographical location. One or more of the authors of this paper self-identifies as a gender minority in their field of research. One or more of the authors of this paper received support from a program designed to increase minority representation in their field of research. While citing references scientifically relevant for this work, we also actively worked to promote gender balance in our reference list.

DECLARATION OF INTERESTS
The authors have no competing interests to declare.

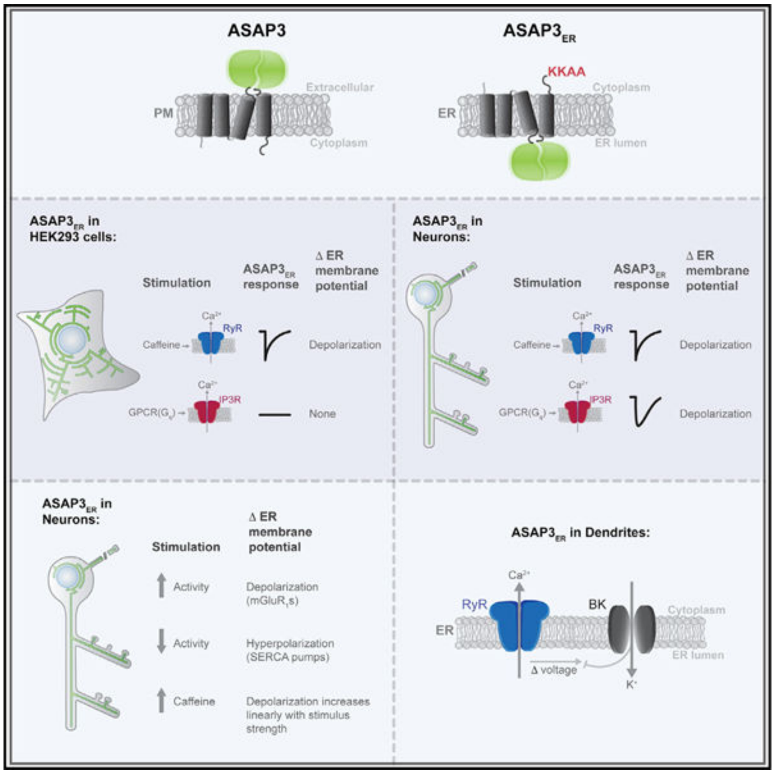

In brief

Recent studies suggest the endoplasmic reticulum (ER) membrane may be electrically active. Campbell et al. retain the genetically encoded voltage indicator ASAP3 to the membrane of the ER and show stimulus-dependent changes in membrane potential in HEK cells and neurons. They further characterize electrical properties of the ER in neurons.

INTRODUCTION

The endoplasmic reticulum (ER) extends throughout a cell as a continuous anastomosing network of membranes.[1–3] Flux of calcium (Ca^{2+}) from the ER lumen into the cytoplasm via IP3 and ryanodine receptors (IP3R and RyR, respectively) is a core function of the ER.[4] Across cell types, the ER has additional resident ion channels, including voltage, ion, and ligand gated channels.[5–12] Moreover, the ionic composition of the ER lumen is distinct from that of the cytoplasm and changes in response to activity, indicating stimulus-dependent movement of ions.[13,14] Yet, ER membrane potential dynamics have not been well characterized.

The ER in neurons is particularly striking as it reaches into axons and dendrites hundreds of microns from the nuclear envelope, where the ER originates.[2,15,16] The ER's channel composition and ionic gradients open the possibility of dynamic electrical signaling. At one extreme, if ER electrical signals actively propagate, this could facilitate rapid intracellular signaling or change the driving force on Ca^{2+} in distant regions of a neuron.[17] At the other extreme, if electrical signals are spatially restricted, this could enable regions of the ER to function independently of adjacent, contiguous segments.

ER ribbons and tubules are tens of nanometers in diameter,[18] prohibiting access with electrodes. Recently, several fluorescent reporters of organelle membrane potential have been developed.[19,20] Optical measurements of ER membrane potential (or sarcoplasmic reticulum, SR) suggest it is polarized and rapidly follows plasma membrane potential,[20–22] but see Sanchez et al.[23] While these reports are intriguing, they are limited by imprecise subcellular targeting of the voltage sensor, uncertainty about the orientation of the sensor (resulting in ambiguity about depolarization and hyperpolarization), or high variability in measurements.

We have selectively targeted the genetically encoded fluorescent voltage indicator, ASAP3,[24] to the ER membrane through the addition of an ER retention sequence (ASAP3_{ER}). Imaging of ASAP3_{ER} in HEK cells reveals RyRs, but not IP3Rs, depolarize the ER membrane. Dissociated neurons from the rat hippocampus have a different repertoire of ER electrical signaling: depolarizing in response to RyR and IP3R activation and changing by tens of millivolts when the activity of cultures are manipulated. Yet, neuronal ER depolarization is linear and spatially restricted, in part through the function of intracellular large conductance K^+ (BK) channels. Thus, we show that while the ER has substantial stimulus-driven changes in membrane polarization, it is a largely passive electrical system with the spread of depolarization limited by additional conductances.

RESULTS

ASAP3 to measure membrane potential

We expressed ASAP3 in HEK cells and calibrated changes in fluorescence with plasma membrane (PM) voltage via whole-cell recordings and simultaneous wide-field epifluorescence imaging (Figure 1A). ASAP3 fluorescence changed linearly, $-1\ \%\Delta F/F$ per 1.9 mV, over a range of physiological voltages (Figures 1B and 1C), consistent with previous reports.[24,25] Fluorescence from an ASAP variant with a non-circularly permuted GFP[24,26] (NCP-ASAP) lacked this voltage sensitivity (Figures 1B and 1C). Thus, ASAP3 linearly reports changes in membrane potential over a range of physiologically relevant voltages.

Targeting and validating ASAP3 at the ER membrane

We next cloned several ER membrane retention peptide sequences[27–30] onto ASAP3 and screened them in HEK cells (Figure S1A). Carboxy terminus tagged ASAP3-KKAA, referred to as ASAP3_{ER}, did not impact cell viability (Figure S1B) and was used going forward. We performed immunostaining to confirm that ASAP3_{ER} is absent from the PM (Figures S1C–S1E), golgi, and mitochondria (Figures S1F–S1H) yet colocalizes with tdTomato in the ER lumen (tdT-ER), unlike ASAP3 or ASAP3 that is targeted to the PM (ASAP3-Kv[24,31]; Figures 1D–1F).

ASAP3$_{ER}$ signals in HEK cells

Does ASAP3$_{ER}$ change fluorescence in response to stimuli that trigger Ca^{2+} release from the ER? Caffeine and Alexa 594, to gate RyRs and visualize the plume, were picospritzed onto HEK cells expressing ASAP3$_{ER}$ (Figure 1G). This triggered a transient decrease in ASAP3$_{ER}$ fluorescence (−5.17 ± 0.55 %ΔF/F, Figure 1H), suggesting an ~10-mV depolarization. Imaging at 10 Hz and 100 Hz showed comparable ASAP3$_{ER}$ responses, indicating the absence of a fast voltage response (Figures 1H and 1I). There was no change in fluorescence when caffeine was puffed onto cells expressing NCP-ASAP targeted to the ER membrane or GFP targeted to the ER lumen (NCP-ASAP$_{ER}$: −0.018 ± 0.048 %ΔF/F; ER-GFP[32]: −0.07 ± 0.053 %ΔF/F; Figures 1H and 1I). Thus, the caffeine-evoked decrease in ASAP3$_{ER}$ fluorescence reflects a bona fide ER membrane depolarization. In separate experiments, cells expressing ER-GECO,[33] a calcium indicator in the ER lumen, decreased fluorescence in response to caffeine, while cells expressing GCaMP6f[34] in the cytoplasm transiently increased in fluorescence (Figures 1L–1N). Together these data indicate that Ca^{2+} efflux through RyRs depolarizes the ER membrane.

Next, we examined the impact of IP3R activation by puffing ligands for G$_q$-coupled receptors onto HEK cells expressing ASAP3$_{ER}$. Neither histamine, gating endogenous histamine receptors,[35] or DHPG, gating exogenously expressed metabotropic glutamate receptors,[36,37] type I (mGluR1) changed ER membrane potential (Figures 1J and 1K). Yet in both cases, we observed an Alexa 594 plume and an increase in cytoplasmic Ca^{2+} (Figures 1O and 1P), indicating delivery of the ligand and Ca^{2+} release from the ER. No change in ASAP3$_{ER}$ or GCaMP6 fluorescence was detected in response to puffing Alexa 594 alone (Figures 1J, 1K, 1O, and 1P), indicating the increase in cytoplasmic Ca^{2+} is not due to mechanical stimulation from the plume. While it surprised us to see ER depolarization in response to RyR but not IP3R activation, the latter is consistent with previous reports[22] and suggests IP3Rs engage additional mechanisms that prevent ER depolarization.

ASAP3$_{ER}$ fluorescence in neurons

In contrast to HEK cells, neurons have elaborate electrical signaling capabilities. To examine whether neuronal ER may be similarly endowed, we first measured the ASAP3 fluorescence-voltage response curve in cultured neurons and confirmed that ASAP3 reliably tracked single action potentials during spontaneous firing (Figures S2A–S2D). As in HEK cells, ASAP3$_{ER}$ colocalized with tdT-ER (Figures S2E–S2G). To visualize ER membrane potential dynamics, we transfected neurons with ASAP3$_{ER}$ and acquired simultaneous imaging and cell-attached recordings, avoiding whole-cell configuration and disruption of the intracellular milieu.[21,23,38] ASAP3$_{ER}$ fluorescence, imaged at 100 Hz, did not rapidly follow action potentials in the PM or generate spontaneous, rapid voltage signals (but see Sepehri Rad et al. and Klier et al.[21,22]) but instead slowly undulated over time (RMSE$_{bsln}$: 3.01 ± 0.540; Figures S2H–S2J). The fluorescence fluctuations were significantly smaller in neurons expressing either NCP-ASAP$_{ER}$ or ER-GFP (RMSE$_{bsln}$: 1.28 ± 0.218 and 1.07 ± 0.177 %ΔF/F, respectively; Figures S2K–S2M). Thus, the ER membrane does not generate fast voltage signals in response to endogenous activity, but it has slower fluctuations evocative of stimulus-evoked changes in membrane potential.

To examine stimulus-evoked changes in ER membrane potential, caffeine or DHPG were focally applied to neuronal somas (Figure 2A). Caffeine evoked a decrease in ASAP3$_{ER}$ fluorescence (−5.41 ± 0.654 %ΔF/F; Figures 2B and 2C), reflecting an ~13-mV depolarization when using the neuronal calibration curve (Figure S2C). Caffeine responses were attenuated by ryanodine (Figure S2N), as expected from the partial block of the receptors.[39,40] Differing from HEK cells, puffing DHPG decreased ASAP3$_{ER}$ fluorescence (−6.52 ± 2.02, Figures 2B and 2C), indicating an ~17-mV depolarization, which was prevented by mGluR antagonists (Figure S2O). Notably, the kinetics of the DHPG-evoked ER voltage responses were significantly slower than those evoked by caffeine (DHPG – rise time: 7.12 ± 2.35 s, decay tau: 11.5 ± 3.34 s; caffeine – rise time: 0.681 ± 0.045 s, decay tau: 2.73 ± 2.03 s; Figure 2C), consistent with protracted G$_q$ signaling. Together with our observations in HEK cells, these findings demonstrate cell-type- and stimulus-specific changes in ER voltage.

Could changes in ER membrane potential be driven by action potentials and synaptic transmission? To test this, we first washed in a high-potassium extracellular solution while simultaneously recording PM electrical activity and imaging somatic ASAP3$_{ER}$. We observed significant decreases in ASAP3$_{ER}$ fluorescence in response to global depolarization that was not observed during prolonged imaging in the standard solution (KCl: −51.5 ± 7.30 %ΔF/F; control: −6.14 ± 2.79 %ΔF/F; Figures 2D and 2G). This suggests the ER membrane potential is capable of depolarizing by as much as ~120 mV.

To determine if more physiologically relevant manipulations of culture activity can change the ER membrane potential, we pharmacologically increased firing and synaptic transmission via bath application of the GABA$_A$ antagonist picrotoxin (PTX). PTX led to a −33.5 ± 3.87 %ΔF/F decrease in ASAP3$_{ER}$ fluorescence, corresponding to an ~80-mV depolarization, while wash in of DMSO alone led to −5.81 ± 0.49 %ΔF/F change (Figures 2E and 2G). Notably, in neurons transfected with NCP-ASAP$_{ER}$ or GFP-ER, the responses to PTX were comparable to ASAP3$_{ER}$ changes from DMSO or with continuous imaging (NCP-ASAP$_{ER}$: −10.5 ± 1.85, GFP-ER: −8.67 ± 2.19 %ΔF/F; Figures 2F and 2G). In contrast, preventing action potentials with bath application of tetrodotoxin (TTX) increased fluorescence (29.6 ± 13.5 %ΔF/F; Figures 2H and 2I), indicating an ~70-mV hyperpolarization. TTX partially reversed the effect of PTX (PTX: −44.6 ± 2.82 %ΔF/F; TTX: 27.33 ± 5.71 %ΔF/F; Figures 2J and 2K). Thus, the ER membrane potential can depolarize or hyperpolarize over many tens of millivolts in response to pharmacological manipulations of neuronal activity.

We hypothesized the hyperpolarization and depolarization observed may be due to Ca^{2+} influx and efflux from the ER lumen, respectively. To test this, we applied thapsigargin to block sarco/endoplasmic reticulum Ca^{2+} ATPases (SERCA) and then washed in TTX. Thapsigargin led to a slow decrease in ASAP3$_{ER}$ fluorescence (−16.2 ± 4.16 %ΔF/F, ~38 mV) and prevented the TTX-associated hyperpolarization (4.7 ± 4.02 %ΔF/F; Figures 2L and 2M). Thus, refilling the ER lumen with Ca^{2+} is a principal component of ER hyperpolarization observed in TTX. Next, we asked if depolarization from PTX could be attributed to Ca^{2+} efflux through IP3Rs. We tested the contributions of G$_q$-coupled mGluRs with bath application of mGluR$_1$ or mGluR$_5$ antagonists (CPCCOEt or MPEP), followed by wash in of PTX. Antagonism of mGluR$_5$ had no impact on the PTX response (−33.3 ± 4.16%ΔF/F, Figures 2N and 2O), but blocking mGluR$_1$ significantly reduced ASAP3$_{ER}$ responses to PTX (−17.4 ± 3.36 %ΔF/F). Blocking both receptor types did not lead to a further reduction (−18.2 ± 3.67 %ΔF/F; Figures 2N and 2O). These data indicate that in hippocampal neurons, mGluR$_1$ activation is a principal driver of ER depolarization associated with stimulation by picrotoxin.

ER membrane potential responses are linear

At the PM, large depolarizations trigger non-linear voltage events. To determine if the ER membrane has similar active properties, we measured ER voltage in response to increasing activation of RyRs by focally applying caffeine (with Alexa 594) for different puff durations (0.1, 0.25, 0.5, and 1 s, applied in random order; Figure 3A). Longer puff durations led to larger changes in the peak ASAP3$_{ER}$ fluorescence (−0.162 ± 0.064, −1.12 ± 0.195, −2.28 ± 0.33, and −5.46 ± 0.643 %ΔF/F, respectively; Figure 3C) that scaled with Alexa 594 fluorescence (Figure 3D) and followed a linear stimulus-response curve. Responses were comparable with 100 Hz and 10 Hz imaging (Figures 3B and 3C). The rate of change in ASAP3$_{ER}$ fluorescence was also largely linear except for the longest puff duration where the measured value plateaued (Figure 3E). Thus, under these conditions, the neuronal ER does not generate superlinear voltage fluctuations, and at the longest stimulus duration, receptor saturation or additional mechanisms may limit depolarization.

Dendritic ER may exhibit different stimulus-dependent voltage responses, owing to regions of low complexity, fewer ribosomes, and different receptor densities.[41–44] We focally applied caffeine to dendrites 50–100 μm from the soma (Figure 3F). Changes in peak ASAP3$_{ER}$ fluorescence scaled with puff duration and Alexa 594 fluorescence (−4.44 ± 1.12, −11.5 ± −2.58, −13.6 ± 1.57, and −19.8 ± 2.55 %ΔF/F, respectively; Figures 3G–3I). The longest caffeine puff, which led to an ~50-mV depolarization, did not trigger a superlinear rate of change in ASAP3$_{ER}$ fluorescence (Figure 3J). Yet responses at dendrites were substantially larger than those at somas (Figure 3K). It is unlikely that this difference is due to mechanics of caffeine delivery or gating of the RyRs as the rise times of the somatic and dendritic responses did not differ (Figure 3L). The decay of the ASAP3$_{ER}$ signal was slower in the dendrites (Figure 3M) but scaled with puff duration (Figure 3N), perhaps reflecting Ca^{2+}-induced Ca^{2+} release. Thus, while we see no evidence of an ER membrane ‘‘action potential,’’ strong activation of RyRs can produce a large amplitude, long-lasting voltage signal.

Electrical potentials in dendritic ER are restricted to stimulated regions

If the ER has a membrane and luminal resistance similar to dendrites,[17] it would have a length constant of ~150 μm (see STAR Methods) and ASAP3$_{ER}$ fluorescence in neighboring segments of dendritic ER would be highly correlated. To examine this, we imaged ASAP3$_{ER}$ or NCP-ASAP in segments of dendrites across consecutive 5-μm bins (Figure 4A). We observed occasional correlations between adjacent bins (Figure 4B), but regions with correlation coefficients (CCs) ≥ 0.75 never extended beyond 15 μm and only spanned 7.31 μm on average. Overall, ASAP3$_{ER}$ signals from neighboring regions of dendrite exhibited low correlation (CC= 0.209 ± 0.032; Figure 4C). In contrast, NCP-ASAP$_{ER}$ fluorescence had significantly higher correlation across all spatial bins (CC = 0.508 ± 0.06; Figures 4D–4F). Thus, ER membrane potential fluctuations are likely highly restricted in space.

To measure the distance over which stimulus-evoked changes in ER membrane potential spread, we puffed caffeine (with Alexa 594) onto dendrites and imaged $\mathrm{ASAP3_{ER}}$ fluorescence over 50 μm (Figure 4G). The peak $\mathrm{ASAP3_{ER}}$ response (−15.7 ± 0.921 %ΔF/F) corresponded spatially with the peak Alexa 594 signal and was comparable to our previous measurements (Figures 4H–4J). The amplitude of the $\mathrm{ASAP3_{ER}}$ response decreased rapidly over short distances, falling to 50% of maximum by ~16 μm and returning to baseline by ~41 μm (Figure 4I). The fluorescence profiles of $\mathrm{ASAP3_{ER}}$ and Alexa 594 showed a near-perfect overlap, indicating that the change in ER voltage is restricted to the regions directly stimulated by caffeine. Indeed, using the stimulus-response curve from dendrites (Figure 3I) and the Alexa 594 profile measured here, we generated an ‘‘expected’’ $\mathrm{ASAP3_{ER}}$ response profile that recapitulates the measured $\mathrm{ASAP3_{ER}}$ signal (CC = 0.959 ± 0.005; Figures 4K and 4L). Thus, there was little to no propagation of ER electrical signals beyond the site of stimulation.

To develop an intuition of how the physical properties of the ER could shape electrical signal propagation, we constructed a passive cable model of the ER that used the average Alexa 594 plume to define the current input at each point and constrained the voltage to a cylinder of various lengths (Figures 4M and 4N; see STAR Methods and supplemental information; Figure S3; Table S1). Our simulations showed that electrotonic spread is insensitive to realistic changes in tubule diameter but strongly influenced by membrane and axial resistance over a range of ER lengths (Figures 4O and S3E–S3G). The model most closely approximated the data when membrane resistance is low and axial resistance is high. Thus, we hypothesized that resident ER ion channels could impact membrane resistance and suppress the spread of stimulus-evoked ER depolarization.

Large conductance K^+ (BK) channels are localized to organelle membranes including the ER,[45] have demonstrated intracellular function,[46–48] and are gated by depolarization and Ca^{2+} as seen with RyR activation. To test if BK channels restrict the spread of ER depolarization, we puffed caffeine onto dendrites, and we compared $\mathrm{ASAP3_{ER}}$ responses before and after application of the cell-impermeant BK channel antagonist iberiotoxin[49] or the cell-permeant antagonists penitrem or paxilline.[50] Blocking PM BK channels had no impact on ER depolarization (Figures 4P and 4Q). In contrast, blocking PM and intracellular BK channels with penitrem reduced the peak ER response and extended the distance over which depolarization was detected (Figure 4R); similar results were obtained in the presence of paxilline (Figures S2Q and S2R). Indeed, the stimulus-evoked depolarization decayed to 50% of the maximum at a greater distance when intracellular BK channels were blocked (Figure 4S). Thus, intracellular BK channels actively suppress the propagation of electrical signals.

DISCUSSION

Our study provides a foundational understanding of electrical signaling in the ER, demonstrating cell type and stimulus specificity, and active regulation of spatial propagation.

By leveraging the localization and orientation imparted by the evolutionarily conserved –KKAA ER retention sequence,[27,51–54] we ensure that photons emitted from $ASAP3_{ER}$ originate from the ER membrane and changes in fluorescence reflect relative depolarizations and hyperpolarizations. While we cannot exclude the possibility that a voltage sensor will have different sensitivities in the ER and plasma membranes, comparing $ASAP3_{ER}$ to $NCP\text{-}ASAP_{ER}$ and GFP-ER abrogates concerns regarding non-voltage-related changes in fluorescence. Moreover, it is unlikely that the –KKAA tag alters the voltage sensitivity of ASAP3, as the larger Kv sequence does not.[24] Thus, our strategy enables measurement of ER membrane potential changes and will be broadly applicable to other cellular systems, such as cardiomyocytes where SR membrane potential remains controversial.[23,55,56]

The IP3R-associated ER depolarization observed in neurons and not HEK cells may reflect the presence of cell-type-specific shunting or rapid counter currents in response to IP3R activation. Alternatively, there may be cell-type-specific differences in the scope of Gq signaling or the single channel properties of IP3Rs. In all cases, this observation reveals heterogeneity in ER electrical signaling and portends cell-type-specific functional consequences for different complements of resident ER ion channels

The ER membrane potential changes slowly, resembling voltage dynamics of other organelles.[19,20] The large changes in voltage we observe are comparable to estimates previously calculated in SR, supporting the need for measurements of ion gradients across the ER (or SR) membrane.[13,14,55] We explored the possibility that large-amplitude ER depolarizations may engage active conductances to generate ER spikes, akin to the summation of synaptic potentials triggering dendritic spikes at the PM.[57] Rather, we find evidence that BK channels restrict electrical responses. This opens the possibility that other ER channels may have similar function,[6,7,56,58–60] giving rise to a compartmentalized ER membrane system where adjacent regions of ER are electrically independent.

The ER has well-characterized subdomains that subserve distinct functions and may exploit compartmentalized electrical signaling. For example, at dendritic branch points the ER increases in structural complexity, restricting protein diffusion, promoting export, and concentrating signaling molecules.[61] These regions have high densities of IP3Rs resulting in Ca^{2+} signaling ‘‘hot spots.’’[62] The surface area and interconnected ER tubules at dendritic branch points may attenuate voltage propagation, exaggerating the compartmentalization. In many cell types, PM-ER contact sites are rich with ion channels that physically and functionally connect the two membranes[63–68]; ER voltage at these sites may influence ion channel function in dramatic ways. Even ER functions that are removed from an obvious link to membrane potential, such as protein folding and protein quality controls, are dysregulated when ER ion channels are mutated.[69,70] Thus, ER electrical signaling should be examined across cell types and ER subdomains to understand the richness of ER function.

Limitations of the study

In this study, we are unable to measure voltage across the ER membrane with respect to a known reference voltage. Thus, the absolute ER membrane potential remains undefined. In addition, our imaging modality cannot resolve ER subdomains, so it is unclear if the changes in voltage reported here occur in specific substructures. This is a particular limitation when imaging ASAP3$_{ER}$ in the soma.

STAR★METHODS

RESOURCE AVAILABILITY

Lead contact—Further information and requests for resources and reagents should be directed to and will be fulfilled by the lead contact, Brenda Bloodgood (blbloodgood@ucsd.edu).

Materials availability—Plasmids generated in this study will be deposited to Addgene and made available with an institutional MTA.

Data and code availability

- All data reported in this paper will be shared by the lead contact upon request.
- All original code has been deposited at Zenodo and is publicly available as of the date of publication. DOIs are listed in the key resources table.
- Any additional information required to reanalyze the data reported in this paper is available from the lead contact upon request.

EXPERIMENTAL MODEL DETAILS

Animals—All animal procedures were performed in accordance with the University of California San Diego Institutional Animal Care and Use Committee (IACUC, protocol number S20032) and complied with all relevant ethical regulations for animal research. Primary hippocampal cultures were prepared from wild-type (WT) Sprague Dawley (Envigo) rat pups on postnatal day 0–1 (P0–1). Hippocampal tissue was collected from animals of both sexes and pooled.

Primary neuronal cultures—Hippocampi from P0–1 rat pups were prepared as previously described.[76] Dissociated neurons were plated at a density of 130 cells per mm^2 on 12 mm diameter glass coverslips coated with poly-d-lysine (Neuvitro, Vancouver, WA). Neurons were continuously maintained at 37°C and 5% CO2 and grown in maintenance media consisting of Neurobasal-A media, supplemented with Glutamax, and B27 supplement (all from Thermo Fisher Scientific, Waltham, MA).

Cell lines—Human embryonic kidney 293 T-variant cells (HEK293T; ATCC, Manassas, VA) were plated on 12 mm glass coverslips (Neuvitro, Vancouver, WA) coated with bovine collagen I (Corning, Corning, NY) according to the manufacturer’s recommendations, and maintained in Dulbecco’s Modified Eagle medium (DMEM) supplemented with 10% fetal bovine serum, and penicillin-streptomycin (all from Thermo Fisher Scientific, Waltham, MA). Cells were continuously maintained at 37°C and 5% CO2 and were passaged at 80–90% confluency. HEK293T are thought to be derived from an epithelial or neuronal lineage from female embryonic human kidney tissue. Our cell line was not authenticated.

METHOD DETAILS

DNA construct subcloning—Plasmids were made by standard molecular biology techniques with all cloned fragments confirmed by sequencing. ASAP3 subcloned into a pcDNA3.1/Puro-CAG vector[72] was provided as a kind gift from Dr. Lin and served as a starting point for cloning putative ER retained ASAP3 variants, which were inserted between Nhe and HindIII restriction sites. The ASAP3 variant containing an amino-terminus MRRR- tag was cloned using 5’′CGCTAGCCGCCACCATGAGGAGGAGGATGGAGACGACTGTGAGGTATGAAC-3’′forward primer with 5’′AAGCTTTCATTAGGTTACCACTTCAAGTTGTTTCTTCTGTG-3’′reverse primer, while variants possessing carboxy-terminus tags all used 5’′CGCTAGCCGCCACCATGGA-3’′forward primer, combined with reverse primers 5’′CAAGCTTTTACGCCGCCTTCTTGGTTACCACTTCAAGTTGTTTCTTCTGTG-3’′ 5’′CAAGCTTTCATTACCTCCTCTTCTTGGTTACCACTTCAAGTTGTTTCTTCTGTG-3’′ or 5’′CAAGCTTTCATTAAGAAGACTTCTTGGTTACCACTTCAAGTTGTTTCTTCTGTG-3’′for -KKAA, -KKRR, or -KKSS retention tags, respectively. The NCP-ASAP construct[24,26], a kind gift from Dr. St-Pierre, was cloned to generate the NCP-ASAP$_{ER}$ control construct using identical -KKAA primers as for ASAP3$_{ER}$. For expression in neurons ASAP3$_{ER}$ was cloned into pAAV-hSyn between NcoI and HindIII restriction sites using 5’′CGTCGACCGCCACCATGGAGACGACT-3’′forward primer and 5’′CCGAGCTCGGTACCAAGCTT-3’′reverse primer.

The pcDNA3.1-Myc-GRM1[73] used to clone pCag-Myc-GRM1-IRES-CyRFP1 was a kind gift from Dr. Banghart and was inserted with an IRES sequence to the pCAG-CyRFP1 vector provided by Dr. Lin. The IRES sequence was inserted using NotI and NcoI restriction sites and GRM1 was inserted between NheI and NotI restriction sites using 5’′CGGAGACCCAAGCTGGCTAGCG-3’′forward primer and 5’′CGCGGCCGCCTACAGGGTGGAAGAGCTTTGCTTGTAG-3’′reverse primer. The CMV-tdTomato-ER-3 was a gift from Michael Davidson (Addgene plasmid #58097; http://n2t.net/addgene:580,97; RRID:Addgene_58097).

Primary neuronal and cell culture transfections—HEK cells were transfected using 1% Polyethylenimine Max (Polysciences Inc., Warrington, PA) according to the manufacturer’s recommendations at approximately 30% confluency and were used for experimentation 2–3 days post-transfection (DPT2–3).

Neurons were transfected with plasmid DNA as indicated using Lipofectamine 3000 (Thermo Fisher Scientific, Waltham, MA) at 6 days *in vitro*(DIV), according to the manufacturer’’ recommendations. Transfected neurons were used for experiments at 9–21 DIV, but specifically from 14–21 for KCl, PTX, or TTX experiments that manipulated activity across cultures.

Trypan Blue viability staining—HEK cells at DPT2–3 were subjected to Trypan Blue stain (Gibco, Life Technologies) according to the manufacturer’’ recommendations. Bright field and 488 fluorescence images were obtained with a Zeiss, Axio Imager.M2 widefield fluorescence microscope equipped with a Zeiss, apotome2 module. Trypan Blue and GFP positivity were scored and % viability was calculated by:

$$\%\ viability = 100\% \times \frac{(\#\ cells\ Trypan\ Blue\ negative\ and\ fluorescence\ positive)}{(\#\ cells\ fluorescence\ positive)}$$

Immunohistochemistry (IHC)—After transfection, HEK cells or dissociated neurons were fixed with warmed (37°C) phosphate buffered saline (PBS) containing 4% paraformaldehyde (Electron Microscopy Sciences, Hatfield, PA) for 10 min. Unless otherwise stated, cells were permeabilized with PBS containing 1% Triton X-100 for 5 in t room temperature. Blocking was performed on ice for 1 h in a PBS solution containing 3% normal goat serum (NGS), 1% bovine serum albumin (BSA), 1% gelatin from cold water fish skin, and 0.1% Triton X-100. Primary antibodies were diluted in PBS solution containing 0.3% NGS, 0.1% BSA, 0.1 % gelatin from cold water fish skin, and 0.1% Triton X-100 and applied to cultures 24 h at 4°C. Secondary antibodies were diluted in the same solution as primaries and were added to cultures at room temperature for 1 h. Coverslips were mounted onto glass slides using DAPI Fluoromount-G mounting media (SouthernBiotechnology, Homewood, AL) to label nuclei. Images were acquired with a Nikon Ti2-E microscope with Nikon A1R HD confocal scanning, equipped with Nikon N-SIM structured illumination and an Andor iXon Ultra 897 EMCCD camera.

For non-permeabilized staining of HEK cells expressing ASAP3 or ASAP3$_{ER}$, cultures were fixed as above, but permeabilization with Triton X-100 was skipped and Triton X-100 was excluded from all solutions. Antibody concentrations and procedures were otherwise identical. For imaging permeabilized and non-permeabilized cultures, microscope and imaging settings were established while imaging permeabilized cultures and were unchanged for subsequent imaging of non-permeabilized cultures.

Electrophysiology—Recordings were obtained at room temperature (~25°C) from HEK cells or cultured rat neurons perfused (2–4 mL per min) with recirculating imaging solution consisting of: 1X HBSS, 25 mM glucose, 10 mM HEPES, 1 mM pyruvate, 0.74 mM Ca-Cl$_2$. Osmolarity and pH were adjusted to 300–310 and 7.3 with double distilled water and NaOH respectively, and solution was sterilized with 0.22 μm filter units (EMD Millipore Temecula, CA). Cells were visualized with infrared differential interference contrast (IR-DIC) and transfected cells were identified by epifluorescence. Patch pipettes (borosilicate glass pipette; Sutter Instruments, CA), with open resistance 3–5 MΩ for whole cell patch experiments and 6–7 MΩ for cell-attached or loose cell patch experiments, were filled with an internal solution consisting of (in mM): 147 K-gluconate, 20 KCl, 10 Na$_2$-phosphocreatine, 10 HEPES, 2 Na-ATP, 0.3 Na-GTP, 5 MgCl$_2$, 0.2 EGTA. Osmolarity was adjusted to 290–300 mOsm and pH to 7.3 with double distilled water and KOH, respectively.

For whole-cell recordings, series resistance (R_s < 30 MΩ) was uncompensated and recordings were discarded if R_s changed by 20% or more. Current-clamp recordings of spontaneous activity in neuron cultures while simultaneously imaging fluorescence at the soma were obtained for 2 min.

For measuring fluorescence responses to various changes in PM potential of HEK cells and cultured neurons, recordings were obtained in voltage-clamp, holding the cell at −65mV. Current was injected (0.5 s pulse duration, three pulses, separated by 5 s) to bring the PM potential to: −85 mV, −75mV, −65 mV, −55 mV, −45 mV, −35 mV, −25 mV, −5 mV, or +15 mV. The order of pulses was provided at random, −75 mV pulses were provided to HEK cells but not neurons. ASAP3 was imaged continuously across all voltage sweeps and fluorescence responses from the soma of neurons or HEK cells were averaged to generate each cell's fluorescence at set voltages. In some recordings, the cell died prior to testing all membrane potential changes, resulting in different n for some membrane potential values.

For spontaneous activity in neuronal cultures or bath applied pharmacology experiments with ASAP3$_{ER}$, NCP-ASAP$_{ER}$, or GFP-ER expressing neurons, loose-patch and cell-attached recordings were performed in current clamp, with an input of 0 pA, from patches with resistances of >100MΩ or <1GΩ, respectively.[36] Neurons were recorded from at DIV14–21 to ensure robust network activity and synaptic maturity. Cells were excluded from analysis if they showed no spontaneous spiking activity or if no change in spiking was observed in response to pharmacology. Spontaneous activity recordings were 2 min; bath application of drugs and continuous imaging controls were 6 min.

Drug application—Activity was manipulated via bath application of the following: 2-Methyl-6-(phenylethynyl)pyridine hydrochloride (MPEP; 1 μM; Tocris Bioscience, Bristol, UK), 7-(Hydroxyimino)cyclopropa[b]chromen-1a-carboxylate ethyl ester (CPCCOEt; 20 μM; Tocris Bioscience, Bristol, UK), Iberiotoxin (20 μM; Tocris Bioscience, Bristol, UK), KCl (40 mM; Sigma-Aldrich, St. Louis, MO), Paxilline (1 μM; Tocris Bioscience, Bristol, UK), Penitrem-A (650 nM; Tocris Bioscience, Bristol, UK), Picrotoxin (PTX; 50 μM; Tocris Bioscience, Bristol, UK), Ryanodine (Ry; 10 μM; Tocris Bioscience, Bristol, UK), sodium tetrodotoxin citrate (TTX; 1 μM; Tocris Bioscience, Bristol, UK), Thapsigargin (thaps; 10 μM; Thermo Fisher Scientific, Waltham, MA), as indicated. Focal drug application was performed through glass pipette, with open resistance of 9.10 MΩ, connected to a Picospritzer II (general valve corporation, Fairfield, NJ) set to minimal pressure (4 PSI). (RS)-3,5-Dihydroxyphenylglycine (DHPG; 500 μM; Tocris Bioscience, Bristol, UK) and caffeine (40 mM; Tocris Bioscience, Bristol, UK) were dissolved neuron imaging media containing Alexa Fluor 594 Biocytin (50 μM; Molecular Probes Inc., Eugene, OR). The pipette tip was placed at a distance of 10 μm from HEK cells, neuron somas or neuron dendrites. DHPG was applied as a single 1 s puff; three puffs of caffeine were applied for the indicated durations with 30 s between puffs. In experiments puffing DHPG onto HEK cells, cells expressing exogenous mGluR1 were identified by red fluorescence from the RFP expressed from the same plasmid, and separated by an IRES sequence. Focal drug applications were repeated while imaging Alexa-594 to visualize application plumes (except for experiments in which cells expressed ER-GECO), and again with DIC to control for mechanical displacement. If mechanical movement was detected in any recording, all recordings for that cell were discarded. Of note, the absolute value of Alexa-594 fluorescence was substantially higher at dendritic regions in comparison to somatic, due to exclusion of the dye from the soma itself

Data acquisition and analysis—Live imaging experiments were performed on an Olympus BX51 wide field epifluorescence microscope (Olympus Life Science Solutions) outfitted with a PCO edge4.2 sCMOS camera (PCO, Kelheim, DE) and Prior Lumen 200 mercury lamp. Excitation and emission filters were used to isolate green (excitation: 473/31 nm, emission: 520/35) and red (excitation: 562/40, emission: 641/75) fluorescence. Excitation light delivery was controlled by a Uniblitz LS6T2–24 shutter and a Uniblitz VMM-D3 driver. Excitation intensity was kept to a minimum (10–25%), except for rapid imaging (100 Hz acquisitions) and imaging of dendrites when intensity was increased. Recordings were obtained with a Multiclamp 700B amplifier (Molecular Devices, Sunnyvale, CA) and National Instruments data acquisition boards (NI PCIe-6259 and BNC-2110; Austin, TX) under control of a 32-bit Windows 7 computer equipped with MATLAB software (Mathworks Inc., Natick, MA) running Scanimage.[74] Physiology data were sampled at 10 kHz and filtered at 6 kHz. Simultaneous optical data were sampled at either 100 Hz or 10 Hz as indicated in the text. Off-ine data analysis was performed using custom software written in MATLAB by E.P.C. or using Neuromatic software (WaveMetrics Igor Pro, Portland, OR). In brief, imaging data were read into MATLAB and used to generate scaled average projection images from all time series images. ROIs were drawn on scaled average projection images by hand delineating cell ROIs (soma or dendrites) and background ROIs. Average intensity values were calculated from background ROIs and subtracted from cell ROIs for every image frame. Imaging time series data was linearly interpolated to fit the physiology data sampling frequency and aligned with respect to time.

Voltage-Fluorescence response curve: To quantify ASAP3 or NCP-ASAP fluorescence at different PM potentials, average fluorescence was calculated for each step and normalized to average baseline fluorescence from 1 s immediately preceding the step. To quantify ASP3_{ER}, $\text{NCP-ASAP}_{\text{ER}}$, or GFP-ER fluorescence during spontaneous activity, imaging data was normalized to the average fluorescence from the entire 2 min recording

RMSE: For calculating the root -mean-square error (RMSE) of the fluorescence in spontaneously active neurons, baseline was calculated from the first 10 s, and used to calculate residuals across 90 s of imaging.

Fluorescence quantification: For experiments calculating change in fluorescence after wash in of a drug, baseline fluorescence was calculated over a 10 s window to account for the fluctuating baseline. Recordings were normalized to this baseline and the response to the manipulation measured over a 1 s window ~240 s after wash-in of the drug. This time window was selected in an effort to allow cells to reach a steady state, without excessive photodamage and maintaining the recording. For focal drug delivery experiments, fluorescence imaging data was generated as above but physiology was not analyzed and imaging data was not interpolated. Imaging data were normalized to baseline fluorescence from 1 s periods directly preceding drug application. Response magnitudes were calculated by fitting an exponential curve to the falling phase of each fluorescence response, beginning at the peak response value, while rise times, and decay constants (τ) were calculated using Neuromatic software.

Fluorescence signals over dendrites with spontaneous activity: For sliding spatial bin analysis along dendritic branch segments during spontaneous network activity, average projection images from across all ASAP3$_{ER}$ images were generated and used to manually draw centerlines for sliding bins along longitudinal axes of dendrites, dendrite ROIs, and background ROIs spanning at least 55 μm along dendrites. Dendrite and background ROIs were subdivided into 11 non-overlapping 5 μm wide bins beginning at the dendrite ROI nearest to the soma. Average ASAP3$_{ER}$ fluorescence intensities were calculated within dendrite and background sliding bin ROIs and corresponding background was subtracted from dendrite ROIs at every image frame. Correlation coefficients were calculated for the ASAP3$_{ER}$ fluorescence from each bin with every other bin and reported in an 11-by-11 matrix via a heatmap color scheme. Correlation coefficient matrices were averaged across cells along respective bins.

Fluorescence signals over dendrites with caffeine application: For sliding spatial bin analysis along dendritic segments with caffeine stimulation, average projection images from across all ASAP3$_{ER}$ images were generated and used to manually draw centerlines for sliding bins along longitudinal axes of dendrites. Alexa-594 average projection fluorescence images were referenced to locate the centroid of drug application on dendrites. Dendrite ROIs and background ROIs were drawn on ASAP3$_{ER}$ average fluorescence projections images, spanning the centroid of drug application and 50 μm along dendrites towardsthe cell body. Dendrite and background ROIs were subdivided into 100 overlapping sliding bins that were 5 μm wide and had centers spaced 0.5 μm apart. Average ASAP3$_{ER}$ fluorescence intensities were calculated within dendrite and background sliding bin ROIs and corresponding background was subtracted from dendrite ROIs at every image frame. Average Alexa- 594 fluorescence intensities were also calculated within dendrite sliding bin ROIs at every image frame. ASAP3$_{ER}$ and Alexa- 594 fluorescence response peaks were determined by fitting an exponential curve to the falling phase of responses, beginning at the peak response value. Timef rames for detecting peak responses were 1 s or less and ranges of exponential fits were adjusted to maximize R^2 values as needed. Maximal ASAP3$_{ER}$ and Alexa- 594 peak responses were plotted at the distances of each spatial bin center. To estimate the distance at which response peaks fell to 50% of the maximum peak at the center of caffeine application, an exponential fit was calculated from the peak vs distance plot of each dendrite.

Confocal and SIM image analysis—Images were analyzed in ImageJ (RRID: SCR_000415; https://imagej.nih.gov/ij/), FIJI (RRID: SCR_002285; https://fiji.sc/) and in custom software written by E.P.C. in MATLAB Images of permeabilized or non-permeabilized HEK cells expressing ASAP3 or ASAP3$_{ER}$ were analyzed in MATLAB. In brief, average intensity projections images were generated, scaled, and used to draw ROIs over transfected cells and background. Average 488 nm and 649 nm fluorescences detected at background ROIs were subtracted from average fluorescences at cell ROIs. Ratios of 649 a.u. 488 a.u. was calculated and normalized to the average 649 a.u. 488 a.u. in permeabilized cells. For assessing colocalization by PCC in HEK cells, the ImageJ ‘‘Coloc 2’’ plugin for FIJI was used on images acquired from a single plane in the z dimension. To assess colocalization in SIM images of neurons by CC, fluorescence profiles were generated in ImageJ software on images from a single plane in the z dimension for 1 μm wide sections through neuron somas between nuclear and proximal dendrite structures, and CCs for profiles were calculated in MATLAB.

QUANTIFICATION AND STATISTICAL ANALYSIS

Mean ± SEM is used as an estimate of center and dispersion of data values throughout this study, with the exception of mean ± SD reported in Figure S2L. For all experiments ‘‘n’’ reports the number of biological replicates. Statistical analysis was performed in Prism software (GraphPad Inc, San Diego, CA). Distributions were assessed with D’Agostino and Pearson normality tests. For data sets with small sample size, normal distributions were assumed. Depending on relationships between experimental populations, significance was determined for experiments with one independent variable by unpaired, paired, or paired ratiometric Student’s t-tests, or by one-way analysis of variance (ANOVA). For experiments with two independent variables two-way ANOVA was performed. Statistical significance was determined when $p< 0.05$.

Mathematical model

Model design: We constructed a 1D partial differential equation model of voltage on the ER membrane, inspired by the linear cable equation.[77,78] We assumed that the cable equation was sufficient to capture the dynamics of the voltage at the ER in response to an input current. The length of the ER was varied along with the ER radius ‘a’ as a free parameter in our simulations. The control radius was taken to be 25 nm.[18] The cable equation was solved for 5 s to capture the spatio-temporal dynamics of voltage across the ER in response to focal caffeine stimulation (Figure 4N). This timescale was chosen to be sufficiently large when compared to the propagation of electrical signals. We assume that the ER membrane is passive and does not actively propagate the voltage signal. We also assume that a change in voltage is proportional to the presence of caffeine along the dendrite. Experimentally we have observed diffusion of the stimulus, caffeine, over time away from the application site. Caffeine activates RyRs in the ER and releases ions from the ER lumen. We used the spatiotemporal dynamics of the Alexa- 594 mixed with caffeine solutions to calculate the stimulus of the model, $I_0(x; t)$ (Figures S3A-S3D).

The cable equation is given by $\frac{\partial V}{\partial t} = \frac{\lambda^2}{\tau}\frac{\partial^2 V}{\partial^2 x} - \frac{V}{\tau} + I_0(x,t)$, where $\tau = C_m R_m$ is the time constant, and $\lambda = \sqrt{\frac{aR_m}{2R_i}}$ is the length constant. The time constant describes how fast the membrane potential responds to ionic currents, while the length constant represents the length that a change in membrane potential will travel along the ER membrane via electrical conduction. C_m is the membrane capacitance (μF/cm^2), R_m is specific membrane resistance (Ω cm^2), R_i is the resistivity of the volume (Ω cm), and a is ER radius (nm).

Model stimulus and fitting: $I_0(x; t)$ represents voltage change due to an injected current from RyR opening as a function of caffeine application. $I_0(x; t)$ is given as

$$I_0(x,t) = \frac{\beta R_m}{a\tau} I(x,t),$$

where β (mA/μm) is a scaling term and $I(x;\ t)$ is a dimensionless function that is obtained from the fluorescence measurements as a function of both x and t.

To obtain $I(x;\ t)$, we plotted all the temporal dynamics of the average Alexa- 594 at each measured spatial bin along the ER (Figure S3A). To simplify the fitting, we fit the decay dynamics of each temporal plot from each trace's maximum value to its return to baseline with an exponential decay function ae^{bt}. The majority of the traces peak at 0.5 s, so that value was taken as the first time of peak for all the fit dynamics. We then mirrored the decay dynamics from 0.5–1 s to 0.5–0 s, such that the fit fluorescence dynamics show a rise to a peak value at 0.5 s then a decay. To make these fits a function of x and t, the coefficients for the exponential decay equations are now fit as a function of space, x. The coefficients a and b are plotted over space and fit as fourth order polynomial functions (see Figures S3B, S3C). Therefore $I(x;\ t)$ has the form $I(x,t) = a(x)e^{b(x)t}$. The reconstructed Alexa- 594 is shown in Figure S3D.

The coefficient a, for the max value, is given by

$$a(x) = -2 \times 10^{-4}x^4 + 0.022x^3 - 0.554x^2 - 5.379x + 270.185$$

The coefficient b, for the decay rate, is given by

$$b(x) = -2.6 \times 10^{-6}x^4 - 2.9 \times 10^{-4}x^3 + 0.01x^2 - 0.052x - 3.917$$

Initial conditions and boundary conditions: The initial condition for voltage is assumed to be zero everywhere. We assume that the caffeine stimulus is applied at x = 0 and can then diffuse out from that location. The boundary condition at x = 0 is prescribed as a Neumann or no-flux boundary condition, $\left.\frac{\partial V}{\partial x}\right|_{x\ =\ 0} = 0$, and the boundary condition at various distances x = L = 25, 50, 100, and 250 μm is prescribed as V(x = L μm) = 0. The same dynamics occurring along the positive x axes are mirrored on the negative x axes, justifying the Neumann boundary condition at x = 0.

Parameter variations: The model has multiple free parameters, notably C_m, R_m, R_i, and β. C_m is the specific membrane capacitance and represents the fact that the cellular membrane acts as a capacitor since the lipid bilayer separates two electrolytic media.

Because the values for C_m, R_m and R_i are not currently known for the ER membrane, we used four different parameter sets to explore a variety of published parameter values, and approximate realistic parameters in dendrites, see Table S1.

β is a free parameter associated with the current injection that acts as the model stimulus. To deal with the uncertainty with this parameter, we fit β for each parameter set in Table S1 such that the maximum value of voltage at x = 0 for each model with radius of 25 nm is equal to the experimentally determined voltage with $ASAP3_{ER}$.

Numerical solver: All simulations are run in MATLAB 2018b using the pdepe solver. Simulations are run for 5s and output at time intervals of 0.001 s. The ER length was discretized into 0.005 μm increments.

Supplementary Material

Refer to Web version on PubMed Central for supplementary material.

ACKNOWLEDGMENTS

We thank Brittney Trinh and Lara Hagopian for technical contributions, Dr. Michael Lin for ASAP3 and pCAG-CyRFP1, Dr. Francois St-Pierre for NCP-ASAP, Dr. Michael Davidson for tdT-ER, and Dr. Matthew Banghart for pCNA3.1^{+}-GRM1. We also thank Dr. David Kleinfeld (UCSD), Dr. Massimo Scanziani (UCSF), and members of the Bloodgood lab for ongoing discussion and careful reading of the manuscript. This work was supported by a National Defense Science and Engineering Graduate (NDSEG) Fellowship to M.K.B., Air Force Office of Scientific Research FA9550-18-1-0051to P.R, NIH NIBIB T32 EB 9380-8 to E.P.C., and NIH NINDS DP2NS097029 and B.L.B.

REFERENCES

1. Martone ME, Zhang Y, Simpliciano VM, Carragher BO, and Ellisman MH (1993). Three-dimensional visualization of the smooth endoplasmic reticulum in Purkinje cell dendrites. J. Neurosci 13, 4636–4646. [PubMed: 8229189]
2. Terasaki M, Slater NT, Fein A, Schmidek A, and Reese TS (1994). Continuous network of endoplasmic reticulum in cerebellar Purkinje neurons. Proc. Natl. Acad. Sci. USA 91, 7510–7514. [PubMed: 7519781]
3. Dayel MJ, Hom EF, and Verkman AS (1999). Diffusion of green fluorescent protein in the aqueous-phase lumen of endoplasmic reticulum. Biophys. J 76, 2843–2851. [PubMed: 10233100]
4. Ross WN (2012). Understanding calcium waves and sparks in central neurons. Nat. Rev. Neurosci 13, 157–168. [PubMed: 22314443]
5. Miller C (1978). Voltage-gated cation conductance channel from fragmented sarcoplasmic reticulum: steady-state electrical properties. J. Membr. Biol 40, 1–23.
6. Yazawa M, Ferrante C, Feng J, Mio K, Ogura T, Zhang M, Lin PH, Pan Z, Komazaki S, Kato K, et al. (2007). TRIC channels are essential for Ca2+ handling in intracellular stores. Nature 448, 78–82. [PubMed: 17611541]
7. Tanifuji M, Sokabe M, and Kasai M (1987). An anion channel of sarcoplasmic reticulum incorporated into planar lipid bilayers: single-channel behavior and conductance properties. J. Membr. Biol 99, 103–111. [PubMed: 2448472]
8. Duncan RR, Westwood PK, Boyd A, and Ashley RH (1997). Rat brain p64H1, expression of a new member of the p64 chloride channel protein family in endoplasmic reticulum. J. Biol. Chem 272, 23880–23886. [PubMed: 9295337]
9. Kuum M, Veksler V, Liiv J, Ventura-Clapier R, and Kaasik A (2012). Endoplasmic reticulum potassium-hydrogen exchanger and small conductance calcium-activated potassium channel activities are essential for ER calcium uptake in neurons and cardiomyocytes. J. Cell Sci 125, 625–633. [PubMed: 22331352]
10. Ahern GP, and Laver DR (1998). ATP inhibition and rectification of a Ca2+-activated anion channel in sarcoplasmic reticulum of skeletal muscle. Biophys. J 74, 2335–2351. [PubMed: 9591661]
11. Ashrafpour M, Eliassi A, Sauve R, Sepehri H, and Saghiri R (2008). ATP regulation of a large conductance voltage-gated cation channel in rough endoplasmic reticulum of rat hepatocytes. Arch. Biochem. Biophys 471, 50–56. [PubMed: 18187033]

12. Kawano S, Nakamura F, Tanaka T, and Hiraoka M (1992). Cardiac sarcoplasmic reticulum chloride channels regulated by protein kinase A. Circ. Res 71, 585–589. [PubMed: 1323433]
13. Pozzo-Miller LD, Pivovarova NB, Leapman RD, Buchanan RA, Reese TS, and Andrews SB (1997). Activity-dependent calcium sequestration in dendrites of hippocampal neurons in brain slices. J. Neurosci 17, 8729–8738. [PubMed: 9348342]
14. Somlyo AV, Gonzalez-Serratos HG, Shuman H, McClellan G, and Somlyo AP (1981). Calcium release and ionic changes in the sarcoplasmic reticulum of tetanized muscle: an electron-probe study. J. Cell Biol 90, 577–594. [PubMed: 6974735]
15. Tsukita S, and Ishikawa H (1976). Three-dimensional distribution of smooth endoplasmic reticulum in myelinated axons. J. Electron. Microsc 25, 141–149.
16. Spacek J, and Harris KM (1997). Three-dimensional organization of smooth endoplasmic reticulum in hippocampal CA1 dendrites and dendritic spines of the immature and mature rat. J. Neurosci 17, 190–203. [PubMed: 8987748]
17. Shemer I, Brinne B, Tegnér J, and Grillner S (2008). Electrotonic signals along intracellular membranes may interconnect dendritic spines and nucleus. PLoS Comput. Biol 4, e1000036. [PubMed: 18369427]
18. Wu Y, Whiteus C, Xu CS, Hayworth KJ, Weinberg RJ, Hess HF, and De Camilli P (2017). Contacts between the endoplasmic reticulum and other membranes in neurons. Proc. Natl. Acad. Sci. USA 114, E4859–E4867. [PubMed: 28559323]
19. Saminathan A, Devany J, Veetil AT, Suresh B, Pillai KS, Schwake M, and Krishnan Y (2021). A DNA-based voltmeter for organelles. Nat. Nanotechnol 16, 96–103. [PubMed: 33139937]
20. Matamala E, Castillo C, Vivar JP, Rojas PA, and Brauchi SE (2021). Imaging the electrical activity of organelles in living cells. Commun. Biol 4, 389. [PubMed: 33758369]
21. Sepehri Rad M, Cohen LB, Braubach O, and Baker BJ (2018). Monitoring voltage fluctuations of intracellular membranes. Sci. Rep 8, 6911. [PubMed: 29720664]
22. Klier PEZ, Gest AMM, Martin JG, Roo R, Navarro MX, Lesiak L, Deal PE, Dadina N, Tyson J, Schepartz A, and Miller EW (2022). Bioorthogonal, fluorogenic targeting of voltage-sensitive fluorophores for visualizing membrane potential dynamics in cellular organelles. J. Am. Chem. Soc 144, 12138–12146. [PubMed: 35776693]
23. Sanchez C, Berthier C, Allard B, Perrot J, Bouvard C, Tsutsui H, Okamura Y, and Jacquemond V (2018). Tracking the sarcoplasmic reticulum membrane voltage in muscle with a FRET biosensor. J. Gen. Physiol 150, 1163–1177. [PubMed: 29899059]
24. Villette V, Chavarha M, Dimov IK, Bradley J, Pradhan L, Mathieu B, Evans SW, Chamberland S, Shi D, Yang R, et al. (2019). Ultrafast two-photon imaging of a high-gain voltage indicator in awake behaving mice. Cell 179, 1590–1608.e23. [PubMed: 31835034]
25. Cornejo VH, Ofer N, and Yuste R (2022). Voltage compartmentalization in dendritic spines in vivo. Science 375, 82–86. [PubMed: 34762487]
26. Chamberland S, Yang HH, Pan MM, Evans SW, Guan S, Chavarha M, Yang Y, Salesse C, Wu H, Wu JC, et al. (2017). Fast two-photon imaging of subcellular voltage dynamics in neuronal tissue with genetically encoded indicators. Elife 6, e25690. [PubMed: 28749338]
27. Teasdale RD, and Jackson MR (1996). Signal-mediated sorting of membrane proteins between the endoplasmic reticulum and the golgi apparatus. Annu. Rev. Cell Dev. Biol 12, 27–54. [PubMed: 8970721]
28. Gao C, Cai Y, Wang Y, Kang BH, Aniento F, Robinson DG, and Jiang L (2014). Retention mechanisms for ER and Golgi membrane proteins. Trends Plant Sci 19, 508–515. [PubMed: 24794130]
29. Schutze MP, Peterson PA, and Jackson MR (1994). An N-terminal double-arginine motif maintains type II membrane proteins in the endoplasmic reticulum. EMBO J 13, 1696–1705. [PubMed: 8157008]
30. Gaynor EC, Te Heesen S, Graham TR, Aebi M, and Emr SD (1994). Signal-mediated retrieval of a membrane protein from the Golgi to the ER in yeast. J. Cell Biol 127, 653–665. [PubMed: 7962050]

31. Daigle TL, Madisen L, Hage TA, Valley MT, Knoblich U, Larsen RS, Takeno MM, Huang L, Gu H, Larsen R, et al. (2018). A suite of transgenic driver and reporter mouse lines with enhanced brain-cell-type targeting and functionality. Cell 174, 465–480.e22. [PubMed: 30007418]
32. Holbro N, Grunditz A, and Oertner TG (2009). Differential distribution of endoplasmic reticulum controls metabotropic signaling and plasticity at hippocampal synapses. Proc. Natl. Acad. Sci. USA 106, 15055–15060. [PubMed: 19706463]
33. Wu J, Prole DL, Shen Y, Lin Z, Gnanasekaran A, Liu Y, Chen L, Zhou H, Chen SRW, Usachev YM, et al. (2014). Red fluorescent genetically encoded Ca2+ indicators for use in mitochondria and endoplasmic reticulum. Biochem. J 464, 13–22. [PubMed: 25164254]
34. Chen T-W, Wardill TJ, Sun Y, Pulver SR, Renninger SL, Baohan A, Schreiter ER, Kerr RA, Orger MB, Jayaraman V, et al. (2013). Ultrasensitive fluorescent proteins for imaging neuronal activity. Nature 499, 295–300. [PubMed: 23868258]
35. Vetter I, and Lewis RJ (2010). Characterization of endogenous calcium responses in neuronal cell lines. Biochem. Pharmacol 79, 908–920. [PubMed: 19883631]
36. Sugiyama H, Ito I, and Hirono C (1987). A new type of glutamate receptor linked to inositol phospholipid metabolism. Nature 325, 531–533. [PubMed: 2880300]
37. Reiner A, and Levitz J (2018). Glutamatergic signaling in the central nervous system: ionotropic and metabotropic receptors in concert. Neuron 98, 1080–1098. [PubMed: 29953871]
38. Perkins KL (2006). Cell-attached voltage-clamp and current-clamp recording and stimulation techniques in brain slices. J. Neurosci. Methods 154, 1–18. [PubMed: 16554092]
39. Kong H, Jones PP, Koop A, Zhang L, Duff HJ, and Chen SRW (2008). Caffeine induces Ca2+ release by reducing the threshold for luminal Ca2+ activation of the ryanodine receptor. Biochem. J 414, 441–452. [PubMed: 18518861]
40. Chen-Engerer H-J, Hartmann J, Karl RM, Yang J, Feske S, and Konnerth A (2019). Two types of functionally distinct Ca2+ stores in hippocampal neurons. Nat. Commun 10, 3223. [PubMed: 31324793]
41. Broadwell RD, and Cataldo AM (1983). The neuronal endoplasmic reticulum: its cytochemistry and contribution to the endomembrane system. I. Cell bodies and dendrites. J. Histochem. Cytochem 31, 1077–1088. [PubMed: 6309951]
42. Walton PD, Airey JA, Sutko JL, Beck CF, Mignery GA, Südhof TC, Deerinck TJ, and Ellisman MH (1991). Ryanodine and inositol trisphosphate receptors coexist in avian cerebellar Purkinje neurons. J. Cell Biol 113, 1145–1157. [PubMed: 1645737]
43. Takei K, Stukenbrok H, Metcalf A, Mignery GA, Südhof TC, Volpe P, and De Camilli P (1992). Ca2+ stores in Purkinje neurons: endoplasmic reticulum subcompartments demonstrated by the heterogeneous distribution of the InsP3 receptor, Ca(2+)-ATPase, and calsequestrin. J. Neurosci 12, 489–505. [PubMed: 1311032]
44. Krijnse-Locker J, Parton RG, Fuller SD, Griffiths G, and Dotti CG (1995). The organization of the endoplasmic reticulum and the intermediate compartment in cultured rat hippocampal neurons. Mol. Biol. Cell 6, 1315–1332. [PubMed: 8573789]
45. Shruti S, Urban-Ciecko J, Fitzpatrick JA, Brenner R, Bruchez MP, and Barth AL (2012). The brain-specific Beta4 subunit downregulates BK channel cell surface expression. PLoS One 7, e33429. [PubMed: 22438928]
46. Li B, Jie W, Huang L, Wei P, Li S, Luo Z, Friedman AK, Meredith AL, Han MH, Zhu XH, and Gao TM (2014). Nuclear BK channels regulate gene expression via the control of nuclear calcium signaling. Nat. Neurosci 17, 1055–1063. [PubMed: 24952642]
47. Selezneva A, Yoshida M, Gibb A, and Willis D (2021). Nuclear BK channels regulate CREB phosphorylation in RAW264.7 macrophages. Pharmacol. Rep 73, 881–890. [PubMed: 33713314]
48. Kulawiak B, Kudin AP, Szewczyk A, and Kunz WS (2008). BK channel openers inhibit ROS production of isolated rat brain mitochondria. Exp. Neurol 212, 543–547. [PubMed: 18572168]
49. Galvez A, Gimenez-Gallego G, Reuben JP, Roy-Contancin L, Feigenbaum P, Kaczorowski GJ, and Garcia ML (1990). Purification and characterization of a unique, potent, peptidyl probe for the high conductance calcium-activated potassium channel from venom of the scorpion Buthus tamulus. J. Biol. Chem 265, 11083–11090. [PubMed: 1694175]

50. Knaus HG, McManus OB, Lee SH, Schmalhofer WA, Garcia-Calvo M, Helms LM, Sanchez M, Giangiacomo K, Reuben JP, and Smith AB 3rd. (1994). Tremorgenic indole alkaloids potently inhibit smooth muscle high-conductance calcium-activated potassium channels. Biochemistry 33, 5819–5828. [PubMed: 7514038]
51. Dogic D, Dubois A, De Chassey B, Lefkir Y, and Letourneur F (2001). ERGIC-53 KKAA signal mediates endoplasmic reticulum retrieval in yeast. Eur. J. Cell Biol 80, 151–155. [PubMed: 11302519]
52. Andersson H, Kappeler F, and Hauri HP (1999). Protein targeting to endoplasmic reticulum by dilysine signals involves direct retention in addition to retrieval. J. Biol. Chem 274, 15080–15084. [PubMed: 10329713]
53. Vincent MJ, Martin AS, and Compans RW (1998). Function of the KKXX motif in endoplasmic reticulum retrieval of a transmembrane protein depends on the length and structure of the cytoplasmic domain. J. Biol. Chem 273, 950–956. [PubMed: 9422755]
54. Isbert S, Wagner K, Eggert S, Schweitzer A, Multhaup G, Weggen S, Kins S, and Pietrzik CU (2012). APP dimer formation is initiated in the endoplasmic reticulum and differs between APP isoforms. Cell. Mol. Life Sci 69, 1353–1375. [PubMed: 22105709]
55. Oetliker H (1989). Energetical considerations related to calcium release from the sarcoplasmic reticulum in skeletal muscle. Biomed. Biochim. Acta 48, S313–S318. [PubMed: 2757605]
56. Gillespie D, and Fill M (2008). Intracellular calcium release channels mediate their own countercurrent: the ryanodine receptor case study. Biophys. J 95, 3706–3714. [PubMed: 18621826]
57. Losonczy A, and Magee JC (2006). Integrative properties of radial oblique dendrites in hippocampal CA1 pyramidal neurons. Neuron 50, 291–307. [PubMed: 16630839]
58. Wang X-H, Su M, Gao F, Xie W, Zeng Y, Li DL, Liu XL, Zhao H, Qin L, Li F, et al. (2019). Structural basis for activity of TRIC counter-ion channels in calcium release. Proc. Natl. Acad. Sci. USA 116, 4238–4243. [PubMed: 30770441]
59. Buyse G, Trouet D, Voets T, Missiaen L, Droogmans G, Nilius B, and Eggermont J (1998). Evidence for the intracellular location of chloride channel (ClC)-type proteins: co-localization of ClC-6a and ClC-6c with the sarco/endoplasmic-reticulum Ca2+ pump SERCA2b. Biochem. J 330, 1015–1021. [PubMed: 9480924]
60. Gillespie D, Chen H, and Fill M (2012). Is ryanodine receptor a calcium or magnesium channel? Roles of K+ and Mg2+ during Ca2+ release. Cell Calcium 51, 427–433. [PubMed: 22387011]
61. Cui-Wang T, Hanus C, Cui T, Helton T, Bourne J, Watson D, Harris KM, and Ehlers MD (2012). Local zones of endoplasmic reticulum complexity confine cargo in neuronal dendrites. Cell 148, 309–321. [PubMed: 22265418]
62. Fitzpatrick JS, Hagenston AM, Hertle DN, Gipson KE, Bertetto-D’Angelo L, and Yeckel MF (2009). Inositol-1, 4, 5-trisphosphate receptor-mediated Ca2+ waves in pyramidal neuron dendrites propagate through hot spots and cold spots. J. Physiol 587, 1439–1459. [PubMed: 19204047]
63. Liou J, Kim ML, Heo WD, Jones JT, Myers JW, Ferrell JE Jr., and Meyer T (2005). STIM is a Ca2+ sensor essential for Ca2+-store-depletion-triggered Ca2+ influx. Curr. Biol 15, 1235–1241. [PubMed: 16005298]
64. Zhang SL, Yu Y, Roos J, Kozak JA, Deerinck TJ, Ellisman MH, Stauderman KA, and Cahalan MD (2005). STIM1 is a Ca2+ sensor that activates CRAC channels and migrates from the Ca2+ store to the plasma membrane. Nature 437, 902–905. [PubMed: 16208375]
65. Prakriya M, Feske S, Gwack Y, Srikanth S, Rao A, and Hogan PG (2006). Orai1 is an essential pore subunit of the CRAC channel. Nature 443, 230–233. [PubMed: 16921383]
66. Thakur P, Dadsetan S, and Fomina AF (2012). Bidirectional coupling between ryanodine receptors and Ca2+ release-activated Ca2+ (CRAC) channel machinery sustains store-operated Ca2+ entry in human T lymphocytes. J. Biol. Chem 287, 37233–37244. [PubMed: 22948152]
67. Vierra NC, Kirmiz M, Van Der List D, Santana LF, and Trimmer JS (2019). Kv2.1 mediates spatial and functional coupling of L-type calcium channels and ryanodine receptors in mammalian neurons. Elife 8, e49953. [PubMed: 31663850]

68. Thillaiappan NB, Chavda AP, Tovey SC, Prole DL, and Taylor CW (2017). Ca2+ signals initiate at immobile IP3 receptors adjacent to ER-plasma membrane junctions. Nat. Commun 8, 1505. [PubMed: 29138405]
69. Jia Y, Jucius TJ, Cook SA, and Ackerman SL (2015). Loss of Clcc1 results in ER stress, misfolded protein accumulation, and neurodegeneration. J. Neurosci 35, 3001–3009. [PubMed: 25698737]
70. Li L, Jiao X, D'Atri I, Ono F, Nelson R, Chan CC, Nakaya N, Ma Z, Ma Y, Cai X, et al. (2018). Mutation in the intracellular chloride channel CLCC1 associated with autosomal recessive retinitis pigmentosa. PLoS Genet 14, e1007504. [PubMed: 30157172]
71. Lam AJ, St-Pierre F, Gong Y, Marshall JD, Cranfill PJ, Baird MA, McKeown MR, Wiedenmann J, Davidson MW, Schnitzer MJ, et al. (2012). Improving FRET dynamic range with bright green and red fluorescent proteins. Nat. Methods 9, 1005–1012. [PubMed: 22961245]
72. Laviv T, Kim BB, Chu J, Lam AJ, Lin MZ, and Yasuda R (2016). Simultaneous dual-color fluorescence lifetime imaging with novel red-shifted fluorescent proteins. Nat. Methods 13, 989–992. [PubMed: 27798609]
73. Kammermeier PJ, and Yun J (2005). Activation of metabotropic glutamate receptor 1 dimers requires glutamate binding in both subunits. J. Pharmacol. Exp. Ther 312, 502–508. [PubMed: 15466247]
74. Pologruto TA, Sabatini BL, and Svoboda K (2003). ScanImage: flexible software for operating laser scanning microscopes. Biomed. Eng. Online 2, 13. [PubMed: 12801419]
75. Schindelin J, Arganda-Carreras I, Frise E, Kaynig V, Longair M, Pietzsch T, Preibisch S, Rueden C, Saalfeld S, Schmid B, et al. (2012). Fiji: an open-source platform for biological-image analysis. Nat. Methods 9, 676–682. [PubMed: 22743772]
76. Ganker G, and Goslin K (1998). Rat hippocampal neurons in low density culture. In Culturing Nerve Cells (A Bradford Book)
77. Yihe L, and Timofeeva Y (2020). Exact solutions to cable equations in branching neurons with tapering dendrites. J. Math. Neurosci 10, 1. [PubMed: 31993756]
78. Rinzel J, and Rall W (1974). Transient response in a dendritic neuron model for current injected at one branch. Biophys. J 14, 759–790. [PubMed: 4424185]

Highlights

- ER membrane potential is imaged via a genetically encoded voltage indicator, $ASAP3_{ER}$
- ER membrane depolarization is receptor and cell type specific
- Neuronal ER depolarizes and hyperpolarizes in different activity conditions
- ER depolarization is linear and spatially restricted by intracellular BK channels

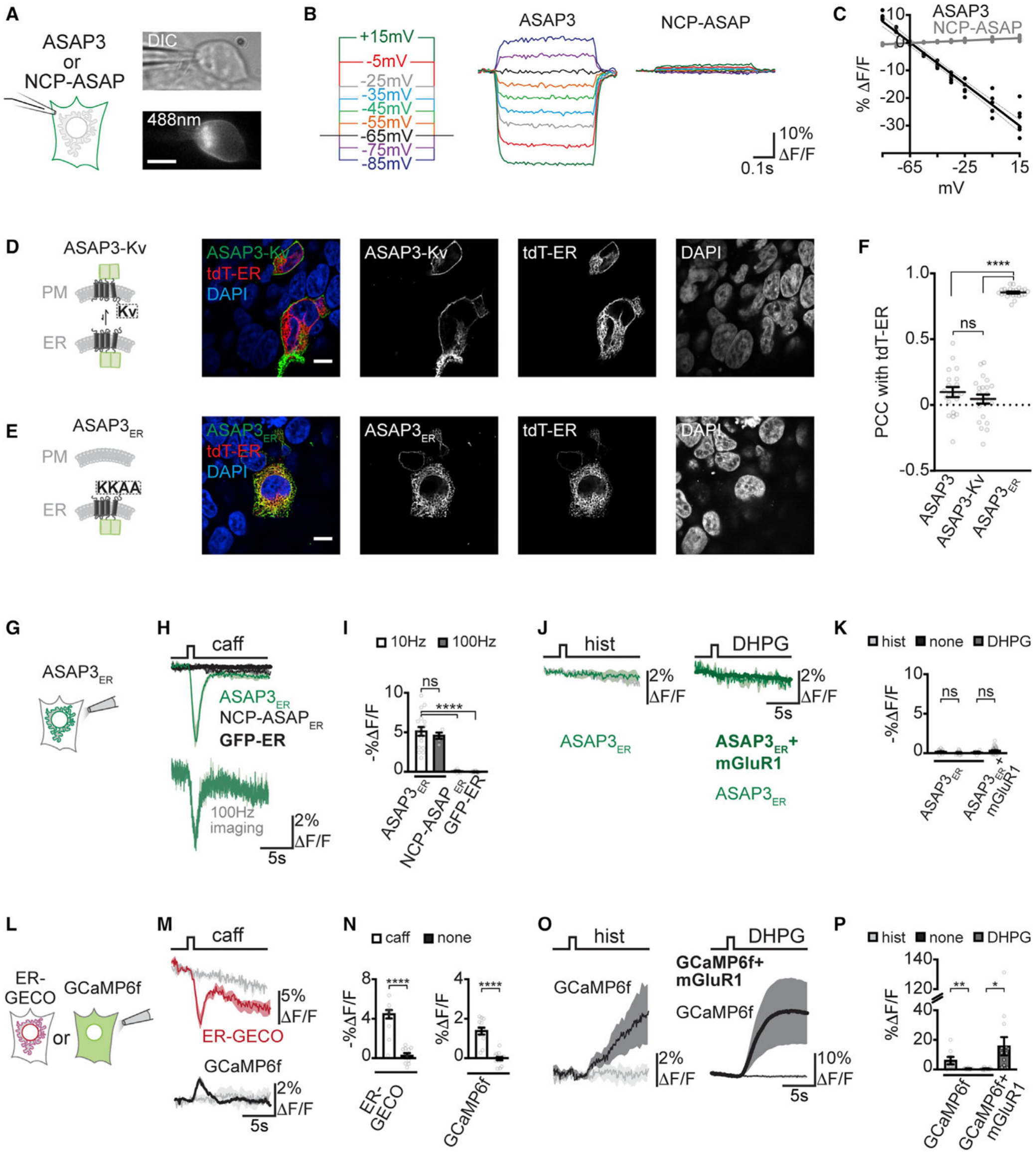

Figure 1. Stimulus-specific changes of ER membrane potential in HEK cells

(A) Schematic of whole-cell and optical recording from an HEK cell expressing ASAP3, DIC, and fluorescence images.

(B) Voltage steps (0.5 s) and corresponding ASAP3 (n = 7) or NCP-ASAP (n = 8) %ΔF/F.

(C) Quantification from (B) (ASAP3: slope = −0.53, $R^2 = 0.99$, NCP-ASAP: slope = 0.032, $R^2 = 0.99$) with linear fit and 95% confidence intervals (CI; dashed lines).

(D) Schematic of ASAP3-Kv subcellular localization and images of a HEK cell expressing tdT-ER and ASAP3-Kv.

(E) As in (D) but ASAP3$_{ER}$.

(F) Quantification of colocalization (Pearson's correlation coefficient = PCC) between tdT-ER and ASAP3 (0.098 ± 0.039; n = 20), ASAP3-Kv (0.045 ± 0.035; n = 22), or ASAP3$_{ER}$ (0.855 ± 0.007; n = 24).

(G) Schematic of focal drug delivery to an HEK cell expressing ASAP3$_{ER}$.

(H) %ΔF/F responses to 1-s puffs of caffeine (caff; 40 mM) onto HEK cells expressing ASAP3$_{ER}$ (10-Hz imaging, n = 17; 100-Hz imaging, n = 5), NCP-ASAP$_{ER}$ (n = 10), or GFP-ER (n = 9).

(I) Quantification of peaks in (H).

(J and K) as in (H) and (I), but puffs of histamine (hist, 1 mM; n = 12), vehicle (n = 13), or DHPG (500 μM) onto HEK cells expressing ASAP3$_{ER}$ (n = 5), or ASAP3$_{ER}$ and mGluR1 (n = 30).

(L) As in (G) but cells expressing a Ca^{2+} indicator.

(M and N) As in (H) and (I), but cells expressing ER-GECO (caff is red, n = 9; vehicle is gray, n = 10), or GCaMP (caff is black, n = 12; vehicle is gray, n = 14). (O and P) As in (J) and (K), but cells expressing GCaMP6f (hist is black, n = 8; vehicle is gray, n = 14; DHPG black, n = 12), or GCaMP6f and mGluR1 (bolded black; n = 20). Data = avg. +/− SEM; imaging = 10 Hz except (B), (C), and (H) indicated; scale bars represent 10 μm; (F) and 10-Hz data in (I) one-way ANOVA, otherwise t test: *$p < 0.05$, **$p < 0.01$, ****$p < 0.0001$.

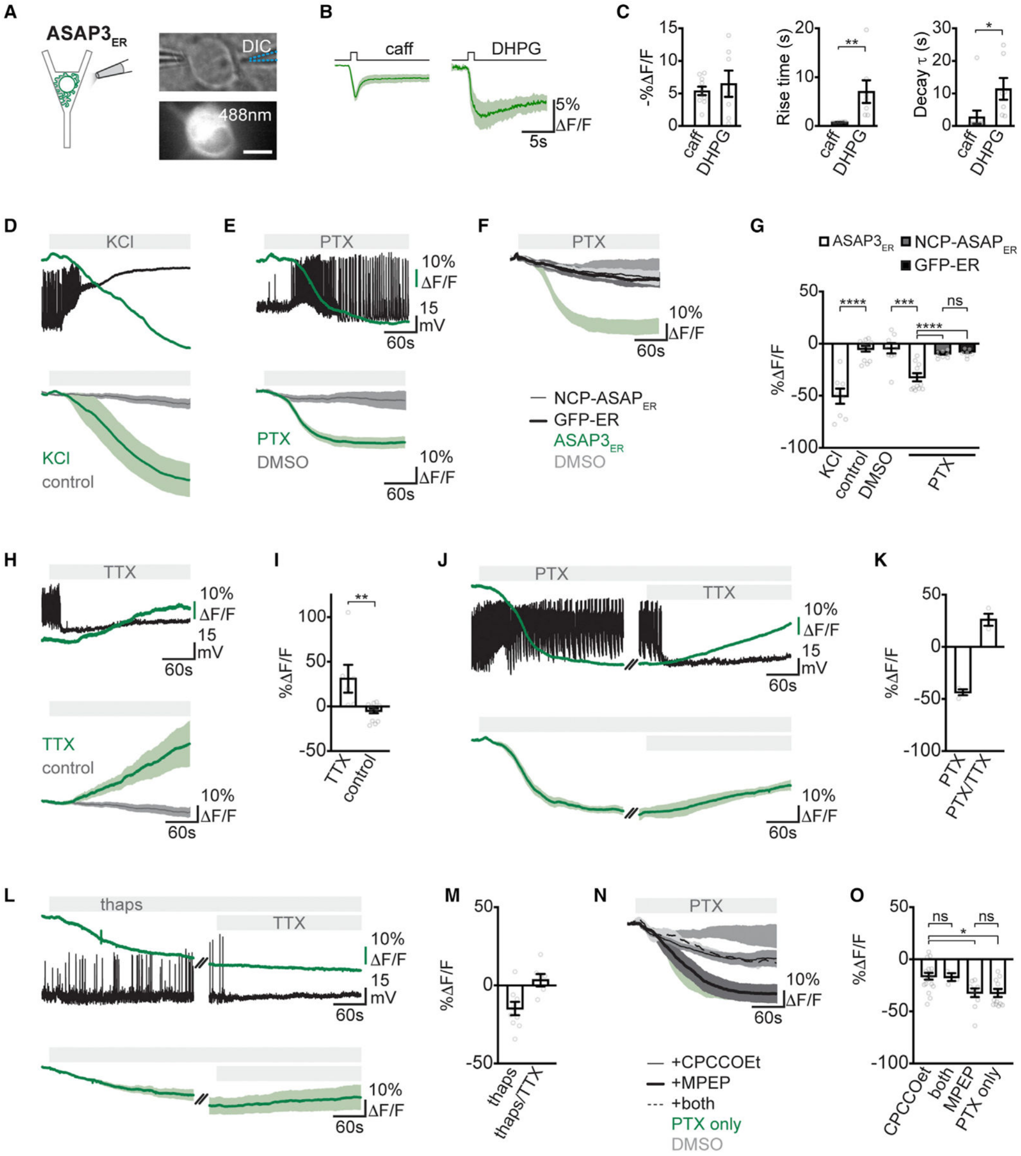

Figure 2. Bidirectional changes of ER membrane potential in neuron somas

(A) Schematic of focal drug delivery to a neuron expressing ASAP3$_{ER}$, with DIC and fluorescence images.

(B) ASAP3$_{ER}$ %ΔF/F during a 1-s puffs of caffeine (n = 10) or DHPG (n = 7).

(C) Quantification of peaks, rise time, and decay time constants (τ) from (B).

(D) Top: example electrical recording (black) and ASAP3$_{ER}$ %ΔF/F (green) during wash in of KCl (40 mM; at gray bar). Bottom: ASAP3$_{ER}$ %ΔF/F during wash in of KCl (n = 8) or continuous imaging (control; n = 12).

(E) As in (D) but picrotoxin (PTX; 50 μM; n = 11) or DMSO vehicle (DMSO; n = 9).

(F) %ΔF/F response of NCP-ASAP$_{ER}$ (n = 8) and GFP-ER (n = 7) to PTX. ASAP3$_{ER}$ PTX and DMSO replotted from (E).

(G) Quantification of (D)–(F).

(H) As in (D) but TTX (1 μM; n = 7) or continuous imaging (replotted from D).

(I) Quantification of (H).

(J) ASAP3$_{ER}$ %ΔF/F during sequential wash in of PTX then TTX.

(K) Quantification of (J) (PTX significance with DMSO $p < 0.001$; TTX significance with control $p = 0.005$).

(L, M) As in (J) and (K) but of thapsigargin (thaps; 10 μM) then TTX (thapsigargin significance with DMSO $p = 0.127$; TTX significance with control $p = 0.771$).

(N) ASAP3$_{ER}$ response to PTX with CPCCOEt (20 μM; $n = 17$), MPEP (1 μM; $n = 10$), or MPEP/CPCCOEt (both; $n = 3$) in the bath. PTX and DMSO replotted from (E).

(O) Quantification of (N). Data = avg. +/− SEM; imaging = 10 Hz; image scale bar represents 10 μm; PTX in (G), and (O) by one-way ANOVA, otherwise t test: $^*p < 0.05$, $^{**}p < 0.01$, $^{***}p < 0.001$, $^{****}p < 0.0001$.

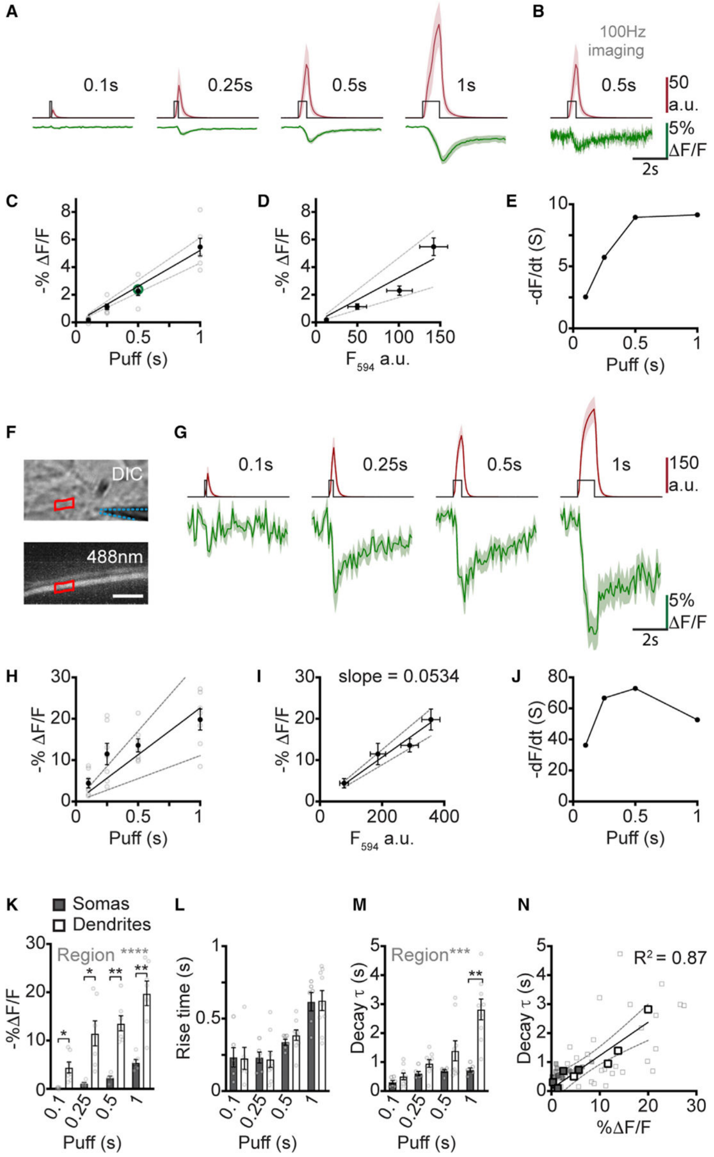

Figure 3. ER membrane potential stimulus-response curves in somas and dendrites

(A) Somatic Alexa 594 and ASAP3$_{ER}$ %ΔF/F during caffeine puffs of indicated durations (n = 6).

(B) ASAP3$_{ER}$ %ΔF/F during a 0.5-s caffeine puff imaged at 100 Hz (n = 3).

(C) Quantification of peaks from (A) and (B) versus puff duration ($R^2 = 0.997$) with linear fit and 95% CI. Green circle is peak from (B).

(D) as in (C) but versus Alexa 594 peaks ($R^2 = 0.909$).

(E) Rate of change of average ASAP3$_{ER}$ responses versus caffeine puff durations.

(F) DIC and fluorescence images of a dendrite expressing ASAP3$_{ER}$. Picospritzer pipette (blue) and region of interest (ROI, red) are indicated.

(G) As in (A) but for dendrites n = 9.

(H–J) As in (C)–(E) but for dendrites (H, $R^2 = 0.897$; I, $R^2 = 0.996$).

(K–M) Quantification of somatic and dendritic ASAP3$_{ER}$ peaks (K), rise times (L), and decay τ values (M).

(N) Decay τ vs. peak for somatic and dendritic ROIs (n = 15). Data = avg. +/− SEM; imaging = 10 Hz unless indicated. Image scale bar represents 10 μm; two-way ANOVA: *p < 0.05, **p < 0.01, ***p < 0.001, **** p < 0.0001. Region in (K) and (M) represents significance between somatic and dendritic ASAP3$_{ER}$ responses. Puff duration significant across both regions in (K–M) p < 0.0001.

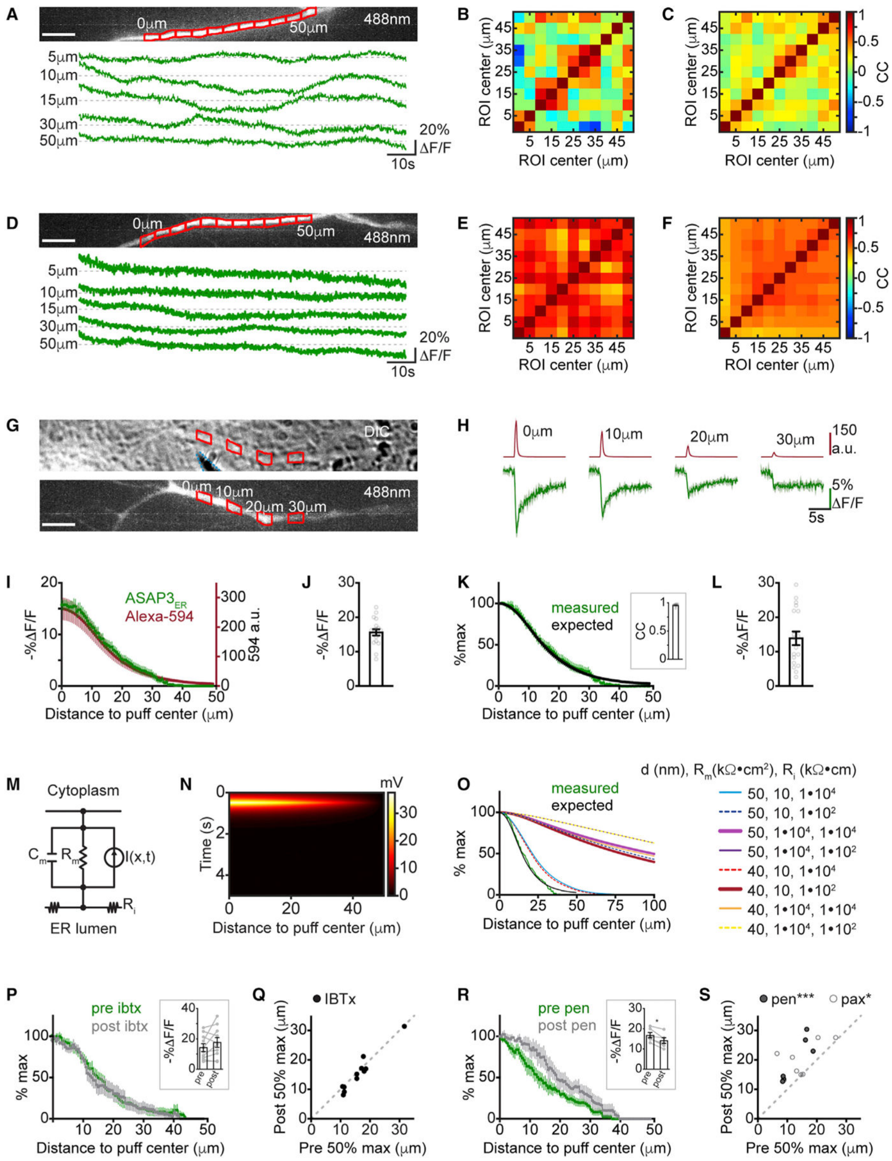

Figure 4. Highly compartmentalized stimulus-evoked changes in dendritic ER membrane potential

(A) Fluorescence image of dendrite expressing ASAP3$_{ER}$. ROIs (red; 5 µm) spanning 50 µm are shown. ASAP3$_{ER}$ %ΔF/F (green) from indicated bins during spontaneous activity.

(B) Example matrix of correlation coefficients (CCs) for ASAP3$_{ER}$ %ΔF/F from ROIs in (A).

(C) Average matrix of CCs (n = 11, 1 dendrite/neuron).</p/>(D–F) As in (A)–(C) but expressing NCP-ASAPER (significance with ASAP3$_{ER}$ CCs p = 0.0002).

(G) DIC and fluorescence images of a dendrite expressing ASAP3$_{ER}$. Picospritzer pipette (blue) and 4 of 100 sliding-bin ROIs (red; 5µm) are shown.

(H) Alexa 594 (red) or ASAP3$_{ER}$ (green) %ΔF/F from indicated ROIs during a 0.5-s puff of caffeine (n = 18).

(I) Spatial profile of ASAP3$_{ER}$ and Alexa 594 peaks across all ROIs (n = 18).

(J) Quantification of ASAP3$_{ER}$ peaks at puff centers.

(K) Normalized, spatial profile of ASAP3$_{ER}$ peaks (measured) or profile expected from Alexa 594 fluorescence (expected; calculated from slope in Figure 3I). Inset: CCs between ‘‘measured’’ and ‘‘expected’’ profiles.

(L) As in (J) but for expected peaks.</p/>(M) Circuit diagram of an ER passive cable model: membrane capacitance = C_m, membrane resistance = R_m, luminal resistivity = R_i, and an injected current = I(x,t).

(N) Example model results of peak voltage across time and distance, using an ER diameter (d) of 50 nm and parameter set 1 (see Table S1 for details).

(O) Model predictions for different d, R_m, and R_i values, ER tubule with length of 250 μm.

(P) Spatial profile of ASAP3$_{ER}$ peaks, 0.5-s puff of caffeine, before and after wash in of iberiotoxin (ibtx; 20 nM; n = 10); normalized to peak at puff center. Inset: quantification of peaks at puff center.

(Q) Distance at which peaks in (P) are 50% max.</p/>(R) As in (P) but wash in of penitrem (pen; 650 nM; n = 6).</p/>(S) As in (Q) but for penitrem and paxiline (pax; 1 μM; n = 8). Data = avg. +/− SEM; imaging = 10 Hz; image scale bars represent 10 μm; ratiometric t test: *$p < 0.05$, ***$p < 0.001$.

KEY RESOURCES TABLE

REAGENT or RESOURCE	SOURCE	IDENTIFIER
Antibodies		
Chicken polyclonal anti-GFP	ThermoFisher Scientific	Cat# A10262; RRID: AB_2534023
Rabbit polyclonal anti-GOLGA2	Proteinetech	Cat# 11308–1-AP; RRID: AB_2115327
Rabbit polyclonal anti-TOMM20	Proteinetech	Cat# 11802–1-AP; RRID: AB_2207530
Goat anti-Chicken AlexaFluor 647	ThermoFisher Scientific	Cat# A-21449; RRID: AB_2535866
Goat anti-Chicken AlexaFluor 488	ThermoFisher Scientific	Cat# A-11039; RRID: AB_2534096
Goat anti-Rabbit AlexaFluor 647	ThermoFisher Scientific	Cat#A-21244; RRID: AB_2535812
Bacterial and virus strains		
E. coli: JM109	Promega	Cat# L2005
Chemicals, peptides, and recombinant proteins		
Picrotoxin (PTX)	Tocris Bioscience	Cat# 1128
2-Methyl-6-(phenylethynyl)pyridine hydrochloride (MPEP)	Tocris Bioscience	Cat# 1212
7-(Hydroxyimino)cyclopropa[b]chromen-1a-carboxylate ethyl ester (CPCCOEt)	Tocris Bioscience	Cat# 1028
Ryanodine (Ry)	Tocris Bioscience	Cat# 1329
(RS)-3,5-Dihydroxyphenylglycine (DHPG)	Tocris Bioscience	Cat# 0342
3,7-Dihydro-1,3,7-trimethyl-1H-purine-2,6-dione (Caffeine)	Tocris Bioscience	Cat# 2793
Tetrodotoxin Citrate (TTX)	Tocris Bioscience	Cat# 1069
Biocytin AlexaFluor594, sodium salt (AlexaFluor594)	Molecular Probes	Cat# A12922
Trypan Blue Stain	Gibco	Cat# 15250–061
Thapsigargin	Thermo	Cat# T7459
Iberiotoxin	Tocris Bioscience	Cat# 1086
Experimental models: Cell lines		
Human: HEK293T	ATCC	Cat# CRL-3216; RRID:CVCL_0063
Experimental models: Organisms/strains		
Rattus norvegicus: Sprague Dawley	Envigo	Cat# 240F
Oligonucleotides		
Primer: pCAG-WT Forward: CGCTAGCCGCCACCATGGA	This paper	N/A
Primer: pCAG-WT Reverse: AAGCTTTCATTAGGTTACCACTTCAAGTTGTTTCTTCTGTG	This paper	N/A
Primer: pCAG-MRRR Forward: CGCTAGCCGCCACCATGAGGAGGAGGATGGAGACGACTGTGAGGTATGAAC	This paper	N/A

REAGENT or RESOURCE	SOURCE	IDENTIFIER
Primer: pCAG-KKAA Reverse: CAAGCTTTTACGCCGCCTTCTTGGTTACCACTTCAAGTTGTTTCTTCTGTG	This paper	N/A
Primer: pCAG-KKRR Reverse: CAAGCTTTCATTACCTCCTCTTCTTGGTTACCACTTCAAGTTGTTTCTTCTGTG	This paper	N/A
Primer: pCAG-KKSS Reverse: CAAGCTTTCATTAAGAAGACTTCTTGGTTACCACTTCAAGTTGTTTCTTCTGTG	This paper	N/A
Primer: hSyn Forward: CGTCGACCGCCACCATGGAGA CGACT	This paper	N/A
Primer: hSyn Reverse: CCGAGCTCGGTACCAAGCTT	This paper	N/A
Primer: GRM Forward: CGGAGACCCAAGCTGGCTAGCG	This paper	N/A
Primer: GRM Reverse: CGCGGCCGCCTACAGGGTGGAAGAGCTTTGCTTGTAG	This paper	N/A
Recombinant DNA		
Plasmid: pCAG-backbone	Lam et al.[71]	Addgene 40257; RRID:Addgene_40257
Plasmid: Puro-CAG-CyRFP1	Villette et al.[72]	N/A
Plasmid: Puro-CAG-ASAP3	Villette et al.[24]	N/A
Plasmid: hSyn-ASAP3	Villette et al.[24]	Addgene 132331; RRID:Addgene_132331
Plasmid: Puro-CAG-ASAP3Kv (pCAG-ASAP3-Kv)	Villette et al.[24]	N/A
Plasmid: pAAV-hSyn-ASAP3Kv-WPRE (hSyn-ASAP3-Kv)	Villette et al.[24]	Addgene 132332; RRID:Addgene_132332
Plasmid: Puro-CAG-ASAP1-NCP (pCAG-NCP-ASAP)	Chamberland et al.[26]	N/A
Plasmid: CMV-LAR-GECO1	Wu et al.[33]	Addgene 61244; RRID:Addgene_61244
Plasmid: pAAV-CAG-GCaMP6f-WPRE-SV40	Chen et al.[34]	Addgene 100836; RRID:Addgene_100836
Plasmid: pcDNA3.1+-Myc-GRM1	Kammermeier et al.[73]	N/A
Plasmid: CAG-Myc-GRM1-IRES-RFP	This paper	Addgene 195355
Plasmid: CMV-tdTomato-ER-3 (CMV-tdT-ER)	A gift from Michael Davidson	Addgene 58097; RRID:Addgene_58097
pMH4-SYN-EGFP-ER	Holbro et al.[32]	Addgene 22285; RRID:Addgene_22285
pCAG-ASAP3-KKAA (pCAG-ASAP3$_{\text{ER}}$)	This paper	Addgene 195356
pAAV-hSyn-ASAP3-KKAA-WPRE (hSyn-ASAP3$_{\text{ER}}$)	This paper	Addgene 195358
Puro-CAG-ASAP3-KKRR	This paper	N/A
Puro-CAG-ASAP3-KKSS	This paper	N/A
Puro-CAG-MRRR-ASAP3	This paper	N/A
Puro-CAG-NCP-ASAP$_{\text{ER}}$	This paper	Addgene 195357
Software and algorithms		
MATLAB (R2009b)	Mathworks Inc	https://www.mathworks.com/
ScanImage	Pologruto et al.[74]	http://scanimage.vidriotechnologies.com/display/SIH/ScanImage+Home
Igor Pro	WaveMetrics	https://www.wavemetrics.com/
Fiji	Schindelin et al.[75]	RRID: SCR_002285; https://fiji.sc/

REAGENT or RESOURCE	SOURCE	IDENTIFIER
ImageJ	Schindelin et al.[75]	RRID: SCR_000415; https://imagej.nih.gov/ij/
Illustrator CC	Adobe Systems Inc.	https://www.adobe.com/products/illustrator.html
Prism	GraphPad Inc.	https://www.graphpad.com/scientific-software/prism/
Original MATLAB code for image analysis	This paper	https://doi.org/10.5281/zenodo.7396643
Original MATLAB code for computational model	This paper	https://doi.org/10.5281/zenodo.7407566
Other		
PDL coated German coverslips	Neuvitro Corporation	GG-12-PDL-Ulaval
DAPI Fluoromount-G®	SouthernBiotech	Cat# 0100–20